Manufacturing and characterization of *in-situ* alloyed Ti6Al4V(ELI)-3 at.% Cu by laser powder bed fusion

A.M. Vilardell[a,*], I. Yadroitsev[b], I. Yadroitsava[b], M. Albu[c], N. Takata[d], M. Kobashi[d], P. Krakhmalev[a], D. Kouprianoff[b], G. Kothleitner[c,e], A. du Plessis[f,g]

[a] *Department of Engineering and Physics, Karlstad University, SE-651, Sweden*
[b] *Department of Mechanical Engineering and Mechatronics, Central University of Technology, Bloemfontein, Free State, 9300, South Africa*
[c] *Graz Center for Electron Microscopy (ZFE), Steyrergasse 17-3, A-8010, Graz, Austria*
[d] *Department of Materials Process Engineering, Graduate School of Engineering, Nagoya University, Furo-cho, Chikusa-ku, Nagoya, 464-8603, Japan*
[e] *Institute of Electron Microscopy and Nanoanalysis, Graz University of Technology, Steyrergasse 17-3, A-8010, Graz, Austria*
[f] *Research Group 3D Innovation, Stellenbosch University, Stellenbosch, Western Cape, 7602, South Africa*
[g] *Department of Mechanical Engineering, Nelson Mandela University, Port Elizabeth, 6001, South Africa*

ARTICLE INFO

ABSTRACT

Biofunctionalization of Ti6Al4V alloy with metallic agents like Ag or Cu is a promising approach to add antibacterial properties and thus to reduce the risk of implant failure. This research investigates the *in-situ* alloying of Ti6Al4V(ELI) with 3 at.% Cu powders using Laser Powder Bed Fusion (L-PBF). The morphology and geometrical characteristics of the single tracks and layers were studied. Laser powers of 170 W and 340 W, and scanning speeds ranging from 0.4 to 1.4 m/s and 0.8–2.8 m/s were implemented. Single track results showed balling effect and humping at high scanning speeds, 1.4 m/s and 1.6 m/s, for each laser powder respectively. Conversely, keyhole formation occurred at lower scanning speeds of 0.4–0.6 m/s for 170 W laser power, and below and 0.8 m/s for 340 W laser power. For both laser powers, single layers resulted in smoother surfaces at lower scanning speeds. These results were used for the development of optimal process parameters for 3D cubes with 99.9 % density. Optimal process parameters were found for 170 W and 340 W laser powders at 0.7 − 0.9 and 1.0–1.2 m/s scanning speeds, respectively.

In-situ alloying by L-PBF was challenging and a homogeneous distribution of Cu within the alloy was hard to achieve. The increase in laser power from 170 to 340 W resulted in small increase in homogenization. Microstructural analyses after stress-relieving treatment showed the presence of α' and β phases, as well as CuTi$_2$ intermetallic precipitates. The finer microstructure together with CuTi$_2$ intermetallic precipitates resulted in an increase in hardness. This study demonstrates the potential for printing *in-situ* alloyed Ti6Al4V(ELI)- 3 at.% Cu for biomedical applications. However, further studies are required to determine the effectiveness of antibacterial properties.

1. Introduction

Metallic biomaterials such as stainless steel, titanium and cobalt chromium alloys are widely used for implantable devices for replacement of structural components of the human body. Titanium (Ti) alloys are less susceptible to bacterial adhesion than stainless steel [1], but commercially available Ti alloys do not exhibit antibacterial capability. Bacterial infections associated with implants occur frequently [2,3]. The coating of implants with antibacterial elements, like silver (Ag), zinc (Zn) and copper (Cu), is proven to be a promising approach to prevent bacterial infection [4]. Cu is a well-known antibacterial

element, and is not toxic to the human body in small amounts [5]. Adding antibacterial properties to stainless steels, cobalt-chromium and titanium alloys by the addition of Cu has been reported in several *in-vitro* and *in-vivo* studies [5–12]. The antibacterial effect and cytotoxicity of Ti-Cu alloys are the subject of many current studies. Pure Cu has been identified to have moderate cytotoxicity; however, pure Ti alloyed up to 20 wt.% Cu did not show any level of cytotoxicity [13]. A higher percentage of Cu is more preferable due to a higher bactericidal effect [14], although some authors pointed out that lower Cu percentages are more desirable in terms of mechanical and corrosion properties, since Ti-Cu alloys with low amounts of Cu would have a closer performance to the

---

initial Ti alloy without Cu [15,16]. Ma et al. [7] and Xu et al. [17] have found that the cytocompatibility of Ti6Al4V with $5-6$ wt.% Cu was equivalent to Ti6Al4V alloy, which is generally recognized as a safe material and was approved for biomedical applications. The growth inhibition of *E. Coli* and *S. Aureus*, which are the main pathogenic microbes responsible for implant-related infections [18], was confirmed for LPBF Ti6Al4V(ELI)-1 at.% Cu alloy surfaces [19].

Implants for bone replacements can be manufactured to combine both the biocompatibility of Ti6Al4V material together with antibacterial properties by the addition of Cu at the bone–implant interface to avoid or reduce the risk of bacterial infection and prevent implant failure. The manufacturing of Ti-Cu alloys from a mixture of elemental powders, by the *in-situ* mixing and alloying during the L-PBF manufacturing is an example of such an approach. One of the main advantages of L-PBF is the freedom in design, which is useful for the manufacturing of custom biomedical implants with the desired shape to fit the exact local requirements for bone replacement of the patient. However, the quality of the parts depends on the manufacturing parameters. Thus, a careful selection of process parameters and manufacturing strategies should be performed to avoid formation of porosity and cracks, high surface roughness, as well as reduce high residual stresses and deformation of the 3D part during the L-PBF manufacturing process. This is even more important when using complex designs such as lattice structures for improved bone attachment [20]. To manage these challenges, together with the high cost and specific design of the implants, a qualification process is required and part quality must be validated [21,22].

The printing and optimization of a new material by L-PBF requires several steps. The L-PBF process involves the scanning and melting of metallic particles in a thin powder layer with a moving high power-density laser beam, forming a molten pool which is solidified into a single track. The formation of stable single tracks with optimal penetration depth plays a major role in the quality and mechanical properties of the 3D manufactured parts. The optimization of process parameters should start with laser power and scanning speed, due to their direct influence on the formation of single tracks. Secondly, a suitable hatch distance, along with scanning strategy need to be selected for the manufacturing of layers with a proper surface roughness and morphology, since a single layer will be the substrate for the next delivered powder layer. Finally, for the *in-situ* alloying approach, the molten pool should exist long enough to guarantee sufficient mixing of the components. Thus, specifically for new materials manufactured by *in-situ* alloying by L-PBF, optimal process parameters and appropriate scanning and building strategies should be carefully selected and optimized, and are expected to be different than the parameters for any individual alloy [23].

The feasibility of *in-situ* alloying by L-PBF has been demonstrated by several authors [24,25].The *in-situ* alloying of powder blends by laser beam melting has been used for the synthesis of new materials such as metal matrix composites, intermetallic and nano-structures, mixtures and alloys with unique properties that can be produced only at high thermal gradients and rapid solidification [26–29]. The purpose of this study was to investigate the relationship between the process parameters and microstructural properties of L-PBF parts by *in-situ* alloying of Ti6Al4V(ELI) (grade 23 Titanium alloy) with 3 at.% Cu powder for biomedical applications.

2. Materials and methods

Argon atomized Ti6Al4V(ELI) and Cu powders with spherical morphologies supplied by TLS Technik GmbH & Co. Spezialpulver KG (Germany) were used in this study. The chemical composition of Ti6Al4V(ELI) powder was specified as 89.26 wt.% Ti, 6.31 wt.% Al, 4.09 wt.% V, 0.12 wt.% O. The Cu powder was specified with a purity of 99.9 %. The particle size distribution of both powders was similar: $\emptyset_{10} = 12.6\,\mu m$, $\emptyset_{50} = 22.9\,\mu m$, $\emptyset_{90} = 37.0\,\mu m$, for the Ti6Al4V(ELI)

powder, and $\emptyset_{10} = 9.45\,\mu m$, $\emptyset_{50} = 21.9\,\mu m$, $\emptyset_{90} = 37.5\,\mu m$ for Cu powder. Ti6Al4V(ELI)- 3 at.% Cu powder mixture was done by mixing powders for 1 h by regular manually inverting the metal container. The final powder mixture was dried at 80 °C for 2 h before printing.

To determine the optimal laser power and scanning speed, 3 single tracks of 20 mm length, single layers of 10×10 mm and cubes of $10 \times 10 \times 10$ mm for each set of process-parameters were manufactured by an EOSINT M280 system. Two sets of process parameters were chosen: (i) 170 W laser power and $0.4-1.4$ m/s scanning speeds and, (ii) 340 W laser power and $0.8-2.8$ m/s scanning speeds. Single layers were scanned in the *X* direction by zig-zag pattern (back and forth), meanwhile 3D cubes were scanned with rotation from one layer to the next by 67° which is the standard procedure for the EOSINT M280 system. Therefore, the powder layer thickness in L-PBF for the first and further layers is different and is defined as a combination of the distance moved by the build platform in the Z-direction (nominal layer thickness), and the morphology of the previously processed layer. Considering the apparent density of loose powder layer (about 50 %), and 30 μm Z movement of the build platform, the actual layer thickness after deposition of several layers during the L-PBF process will be about $45-50\,\mu m$. Thus, in order to have similar actual powder layer thickness, for the experiments with single tracks and single layers, the powder thickness of 50 μm was used, meanwhile 3D samples were built at 30 μm- nominal thickness. The manufacturing was performed on Ti6Al4V substrates of 3 mm thickness under protected Ar atmosphere, with an oxygen content less than 0.07 %. The single tracks were investigated from top view (a minimum of 6 measurements for width of the track). Later on, single tracks were cross-sectioned perpendicularly to the scanning direction and width and penetration depth were studied (6 cross-sections were analyzed for process-parameters). The top surface of the single layers was investigated by surface roughness profilometer perpendicularly to the scanning direction, then cross-sectioned single layers were also investigated. The 3D samples attached to the baseplate were heat treated in a vacuum furnace for 3 h at 650 °C for stress relieving. Subsequently, samples were cut from the substrate by wire-cut electrical discharge machine.

X-ray micro computed tomography (microCT) was employed to study the porosity of manufactured samples. MicroCT scans were performed at the Stellenbosch CT facility (Stellenbosch University, South Africa) with data visualization and analysis performed in Volume Graphics VGSTUDIO MAX 3.1. The use of microCT in additive manufacturing was reviewed comprehensively in [21] where the imaging of porosity and inclusions was discussed. In this work, samples subjected to scanning were $10 \times 10 \times 4$ mm in size, with scan parameters 200 kV and 70 μA, with a voxel size of 15 μm and 2400 images recorded in a full rotation of the sample. The data was processed according to guidelines in [30].

The microstructure of samples was studied by optical and scanning electron microscopies (OM, SEM). OM was carried out with AxioVision and SmartZoom (Zeiss) microscopes. SEM was carried out with a LEO 1350 FEG operated at 20 kV. High-resolution scanning transmission electron microscopy (HR-STEM) was performed for deeper microstructural investigations by using a FEI Titan 3 G2 60–300 STEM equipped with a Cs corrector operated at 300 keV. The STEM microscope was equipped with a Super X detector (4 Si-drift detectors) for chemical analyses by x-ray spectroscopy. Element mapping and line profiles were acquired and processed with VELOX software [31]. Element quantification was performed by using the K-factor method [32]. HR-STEM sample preparation was performed by argon ion-milling at room temperature. HR-STEM micrographs were recorded with the annular dark field (ADF) and high angular annular dark field (HAADF) detectors and were processed by using the Digital Micrograph software. X-ray diffraction (XRD) measurements were conducted using a Cu-Kα radiation source (wave length $\lambda = 0.15405$ nm) operated at 40 kV and 40 mA to identify constituent phases. A thermodynamic equilibrium calculation for the Ti–Al–V–Cu quaternary system was carried out using

a CALPHAD approach [33]. Based on a thermodynamic database for a Ti-based multi-component system (PanTi) [34] for a composition range of Ti–6 wt.% Al–4 wt.% V (corresponding to a nominal composition of Ti6Al4V ELI)-Cu. Microhardness measurements were conducted on a Future-Tech micro-hardness tester FM at 200 g load and the load time was 15 s.

3. Results

3.1. Development of process parameters of Ti6Al4V(ELI)-3 at.% Cu alloy

The optimization of L-PBF process parameters was carried out according to the procedure described in [23]. Firstly, single tracks were manufactured, and the shapes and geometry of these tracks were assessed. Based on the single track width, penetration depth and shape, and considering the homogeneity of the alloying element, a few sets of process parameters were selected to manufacture the single layers and 3D specimens.

3.1.1. Development of parameters for single tracks

To find the optimal process parameters for Ti6Al4V(ELI)-3 at.% Cu single tracks, experiments were conducted with laser powers of 170 W and 340 W and scanning speeds between 0.4–2.8 m/s on a 50 μm thickness powder layer. The starting process parameters for Ti6Al4V (ELI)-3 at.% Cu were chosen based on a prior study of the optimization of Ti6Al4V(ELI), on the same system [35]. The increase in laser power from 170 to 340 W led to an increase in single track width of approximately $25-50$ μm wider with the same scanning speed (Fig. 1a).
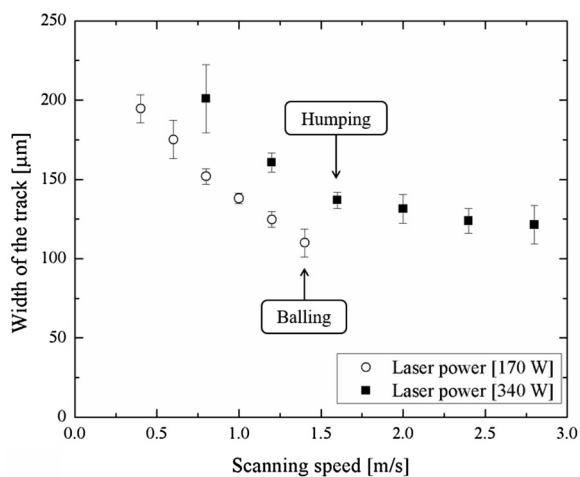
(a)

(b)

Fig. 1. (a) Single track width of Ti6Al4V(ELI)-3 at.% Cu as a function of scanning speed; (b) top view of the Ti6Al4V(ELI)-3 at.% Cu single track with a laser power of 340 W and scanning speed of 1.6 m/s, when humping and balling effects started.

Slow and high scanning speeds resulted in a greater variation of track widths within a single track, which indicates an instability of the molten pool at short and long material interaction times. From analysis of the top view of single tracks at the substrate, it was concluded that: (i) with a laser power of 170 W, the balling effect started at 1.4 m/s scanning speed and, (ii) humping of the molten pool started at 1.6 m/s scanning speed with a laser power of 340 W (Fig. 1b). The single track width was physically limited by the laser beam spot size and flows within the molten pool which are more prominent at higher laser power.

Observations of the single track cross-sections perpendicular to the scanning direction were performed to estimate the L-PBF melting mode and penetration depth of the molten pool. The molten pool depth increased significantly with the increase in laser power, almost double for the same laser scanning speed (Fig. 2a). The analysis of the cross-sections revealed that keyhole mode (trapped keyhole pores) were found at and below scanning speeds of 0.4–0.6 m/s and 0.8 m/s with laser powers of 170 W and 340 W, respectively (Fig. 2a–c). It should also be noted that the depth of penetration was highly variable with a low scanning speed of 0.8 m/s and laser power of 340 W. Humping of the molten pool and undercuts at high scanning speeds were very prominent with higher laser power (340 W). Analysis of top views and cross-sections showed that for 340 W laser power, full fragmentation of the molten tracks (balling effect) did not occur up to scanning speeds of 2.8 m/s.

Investigations of single tracks indicated that continuous line tracks without keyhole pores and balling effect were produced at 170 W and 0.6–1.2 m/s scanning speed and at laser power 340 W higher than 0.6 m/s and lower than 1.4 m/s. Same conditions studied for line tracks were used to print the single layers to show the hierarchical approach used in the present study.

3.1.2. Development of parameters for single layers

For the production of single layers, a hatch distance of 80 μm, lower than the value selected for Ti6Al4V(ELI) without Cu addition (100 μm) was chosen [36]. This helped to remelt a larger portion (40–50 % of single track width) of the previously manufactured single track ensuring better *in-situ* homogenization of the material. Surface topography analyses of the first single layer showed lower surface roughness (Rz = $10-15$ μm) with scanning up to 1.4 m/s with narrow standard deviations, indicating that surfaces were smooth. Conversely, with scanning speeds from 1.6 m/s, the surface roughness increased (as well as their deviations), showing a high level of surface irregularities (Rz = $25-50$ μm) (Fig. 3).

The analysis of the first layer of *in-situ* alloyed material showed the manufacturing of smoother surfaces at lower scanning speeds in ranges between 0.4–1.2 m/s and 0.6–1.4 m/s, for laser powers of 170 W and 340 W, respectively, at the chosen hatch distance of 80 μm. Taking into account the pores and deeper penetrations into the substrate detected during the formation of single tracks at slow scanning speeds between $0.4-0.6$ m/s and the humping/balling effects which started at 1.4 m/s, a reduced matrix of process parameters was suggested for the printing of 3D samples.

3.1.3. Manufacturing of 3D samples

3D samples were built with a laser power of 170 W and 340 W, and scanning speeds between $0.7-0.9$ m/s and 1.0–1.2 m/s respectively, maintaining the hatch distance of 80 μm. The porosity of the manufactured cubes was assessed using microCT method. A maximum pore size of approximately 400 μm was found at the bottom part of the sample that was produced with a laser power of 170 W and scanning speed of 0.9 m/s (Table 1, Fig. 4). No pores were detected for the samples produced with a laser power of 340 W and scanning speed 1.0 m/s at the chosen voxel size by microCT scans. The other samples produced at 340 W had a lower porosity in comparison with the ones produced at 170 W. Small pores had spherical shape and could be
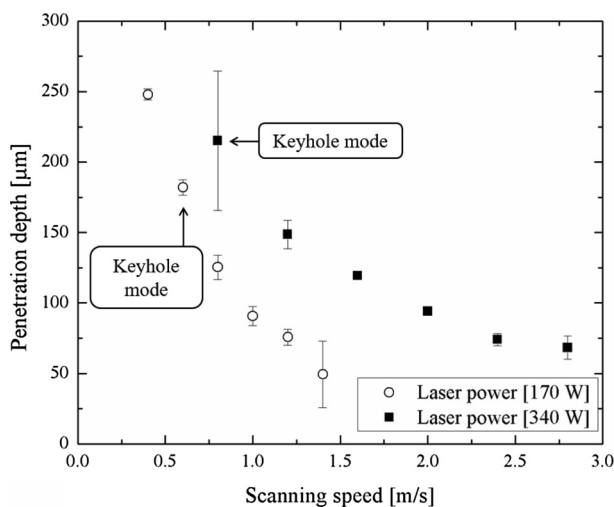
(a)
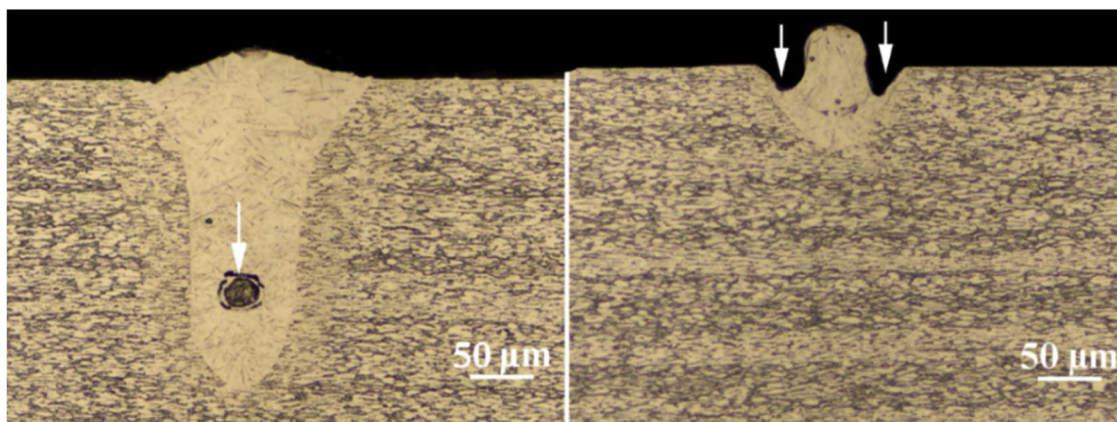
(b)   **(c)**

Fig. 2. (a) Penetration depth of Ti6Al4V(ELI)-3 at.% Cu single tracks *versus* scanning speeds; cross-sections of single tracks manufactured with laser power and scanning speeds of (b) 170 W, 0.4 m/s and, (c) 340 W, 2.8 m/s. (b) Trapped porosity within the melted pool (keyhole mode), and (c) undercuts/grooves formed with the shape of a notch at both sides of the track when humping/balling effects started (indicated by the arrows).
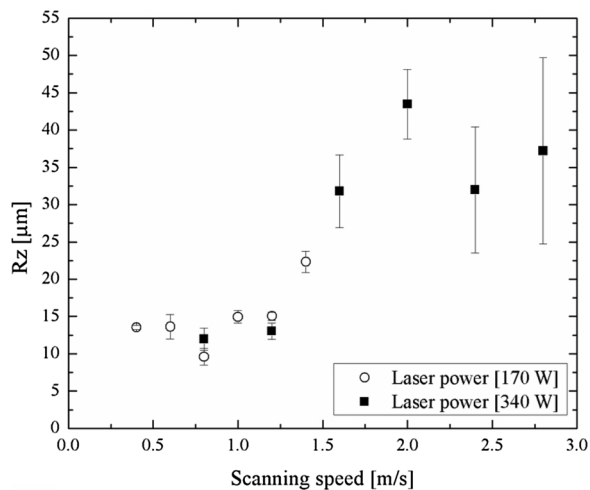

Fig. 3. Surface roughness (Rz) of the first layer versus scanning speed of single layers manufactured with laser powers of 170 W and 340 W.

Table 1
Defect analysis of Ti6Al4V(ELI)-3 at.% Cu samples by microCT scans.

Scanning speed [m/s]	Pore size diameter [Ø]		Porosity [%]
	$\text{Ø}_{min.}$ [mm]	$\text{Ø}_{max.}$ [mm]	
170 W laser power			
0.7	0.0490	0.1061	0.0114
0.8	0.0532	0.3437	0.0165
0.9	0.0490	0.3952	0.0124
340 W laser power			
1.0	–	–	0.0000
1.1	0.0628	0.1122	0.0010
1.2	0.0489	0.2007	0.0099

340 W laser power (Table 1). Actually, high density of 99.9 % revealed by microCT scans was supported by cross-sectioning and microscopic analysis for all cubes (Fig. 4c, d). Thus, optimal process parameters for the 3D *in-situ* alloyed Ti6Al4V(ELI)-3 at.% Cu samples were found to be with laser powers of 170 W and 340 W and scanning speeds of $0.7 - 0.9$ m/s and 1.0–1.2 m/s, respectively.

identified as metallurgical pores [21]. With a laser power of 170 W, pores looked more irregular which indicated a lack-of-fusion. Minimal porosity was found at 170 W, 0.7 m/s scanning speed and 1.0 m/s and
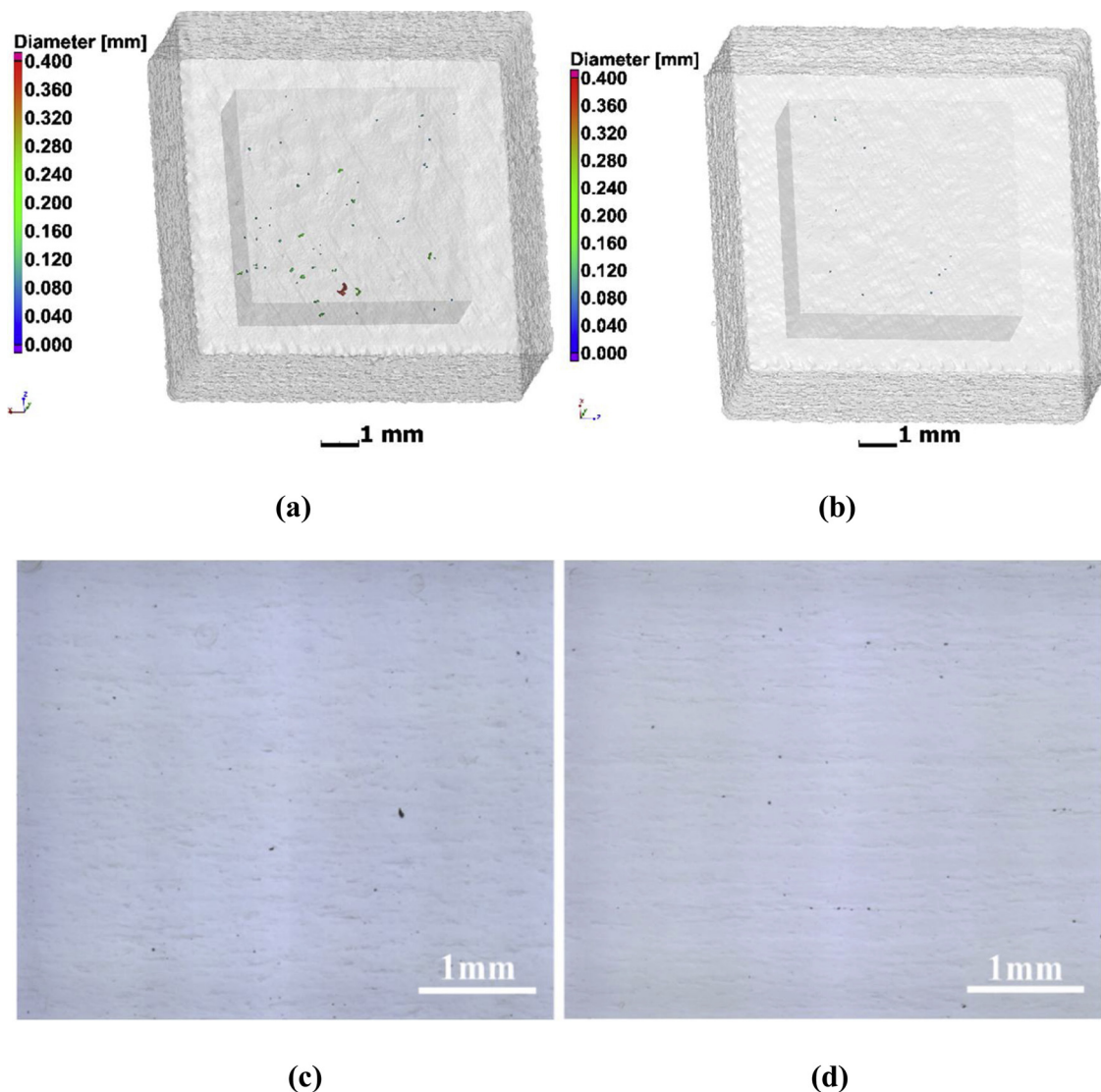
Fig. 4. (a,b) MicroCT scans and (c, d) cross-sections of Ti6Al4V(ELI)-3 at.% Cu samples produced with laser powers and scanning speeds of (a,c) 170 W and 0.9 m/s, and (b, d) 340 W and 1.1 m/s.

3.2. Microstructural analysis of L-PBF Ti6Al4V(ELI)-3 at.% Cu

Chemical homogeneity of the stress-relieved specimens was investigated by SEM and EDX. A typical SEM micrograph in back-scattered electrons (BSE) mode is presented in Fig. 5a. It was observed that the material had chemical inhomogeneity and Cu had a trend to segregate at the bottom of layer fusion boundaries. For the material manufactured with a laser power of 170 W this trend was much more pronounced in comparison with 340 W. The average concentration of Cu in dark regions of the investigated specimens (Fig. 5a) was 3.0–3.7 and 2.1–3.5 wt.% in material manufactured with a laser power and scanning speed of 340 W at 1.0 m/s and 170 W at 0.7 m/s, respectively. Remarkable segregation of Cu at fusion boundaries is illustrated in Fig. 5b. The concentrations of Cu at the fusion boundaries reached $19-23$ wt.% in the material manufactured at 170 W and 0.7 m/s, while in the more homogeneous material manufactured at 340 W and 1.0 m/s, the highest concentration of Cu measured at the fusion boundaries was 9.5–10.5 wt.%, by EDX method. The microstructure of the material had a needle-like morphology, typical to hexagonal α' martensite phase observed in Ti alloys. Nevertheless, compared to the martensite observed in Ti6Al4V(ELI) manufactured by L-PBF [36,37], the needles were finer, which was a result of the different solidification rates caused

by alloying with Cu and different process-parameters.

Deeper microstructural analyses were performed with samples manufactured with a laser power of 170 W and scanning speed of 0.7 m/s. The same microstructural features were observed in the materials manufactured with the other process parameters. CALPHAD was used as an initial approach to simulate the Ti6Al4V-Cu phase diagram, to identify the phases under equilibrium conditions. In a ternary composition of Ti–6 wt.% Al–4 wt.% V, the β-transus temperature was located around 920 °C. The diagram indicated a decrease in β-transus with the addition and increase in Cu content, reaching a β-transus of 820 °C at 4.1 wt.% (3 at.%) Cu (Fig. 6a) due to its β-stabilizer effect. Thus, it can be assumed that the addition of Cu could enhance the formation of retained β-phase during the L-PBF process. At the same time, due to the limited solubility of Cu in α-Ti, an intermetallic $CuTi_2$ phase is formed at 560 °C (3 at.% Cu), leading to a three-phase region area of $α + β + CuTi_2$ [38]. Fig. 6b presents the calculated fractions of the constitute phases (in equilibrium at room temperature of 25 °C) as a function of Cu content (wt.%). The fractions of $CuTi_2$ phases continuously increased with the increase in Cu content, predicting up to approximately 7 mol.% of $CuTi_2$ phase by the addition of 3 at.% Cu. Additionally, a two-phase eutectoid reaction $β→α + CuTi_2$ can be considered to occur at higher Cu content (~14 wt.% Cu) in the Ti–Al–V–Cu
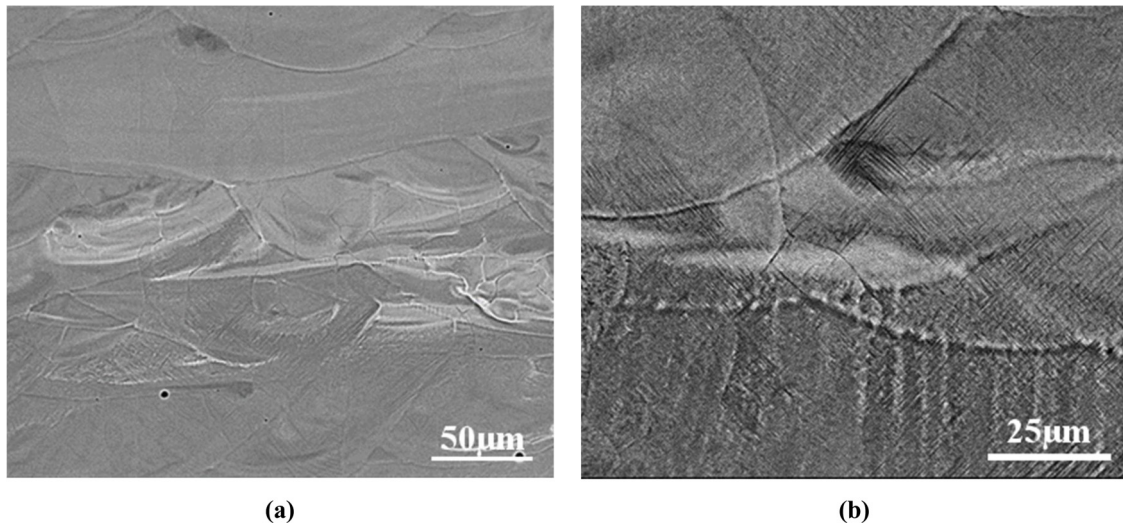
(a)   **(b)**

Fig. 5. SEM BSE micrographs of the Ti6Al4V(ELI)-3 at.% Cu material manufactured with a laser power and a scanning speed of 340 W and 1.0 m/s, (a) low and (b) high magnifications.

quaternary system, previously observed in a Ti–Cu binary system (at 7.1 wt.% Cu) [39]. However, in the present study, the addition of V element (acting as a β-phase stabilizer) resulted in the reduction of eutectoid temperature from 792 °C (Ti-Cu binary phase diagram) down to ~600 °C (Ti6Al4V-Cu quaternary phase diagram) as well as the stabilization of β-phase at lower temperatures, resulting in the presence of three phase region of α + β + CuTi$_2$.

XRD measurements were performed to identify the phases of the *in-situ* alloyed material after stress-relieving heat treatment. Most of the peeks were identified as α/α′-phase (Fig. 7). The presence of the β-phase was not possible to be clearly identified by XRD due to the peak overlap. However, the addition of 3 at.% Cu slightly changed the microstructure of the typical Ti6Al4V(ELI) material. Low intense peaks of CuTi$_2$ phase were found.

General STEM observations showed two regions, low and high-Cu regions, within L-PBF Ti6Al4V(ELI)-3 at.% Cu material (Fig. 8). Fig. 8a shows the first region corresponding to the α′-martensite laths, with a thickness between 0.5–1.5 μm. This first region was observed in the majority of the analyzed areas, and was the dominating one. HADDF imaging allowed the observation of submicrometer precipitates, preferentially located along α′ boundaries but also within them (white arrows, Fig. 8b). The spherical-like shape precipitates showed a homogeneous distribution within the matrix. The precipitates were identified as β-phase and CuTi$_2$ intermetallic precipitates, as illustrated
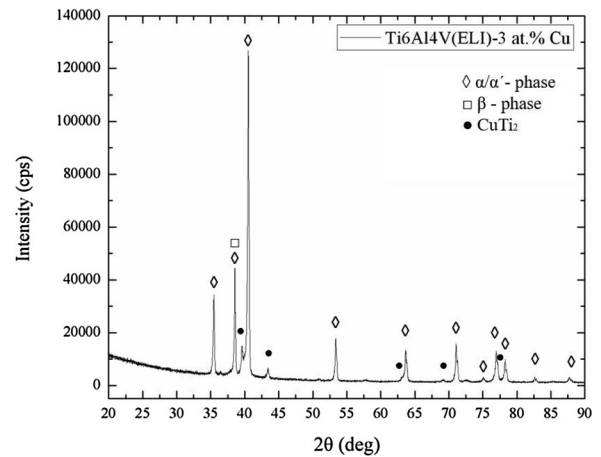

Fig. 7. XRD pattern of L-PBF Ti6AL4V(ELI)-3 at.% Cu manufactured with a laser power of 170 W scanning speed of 0.7 m/s after stress-relieving heat treatment.

in Figs. 9 and 10. The second region showed a coarser microstructure with round α grains of a size between 2 − 10 μm, probably due to partial decomposition of α′-martensite phase towards acicular α by slight coarsening of the microstructure after stress reliving treatment (Fig. 8c-
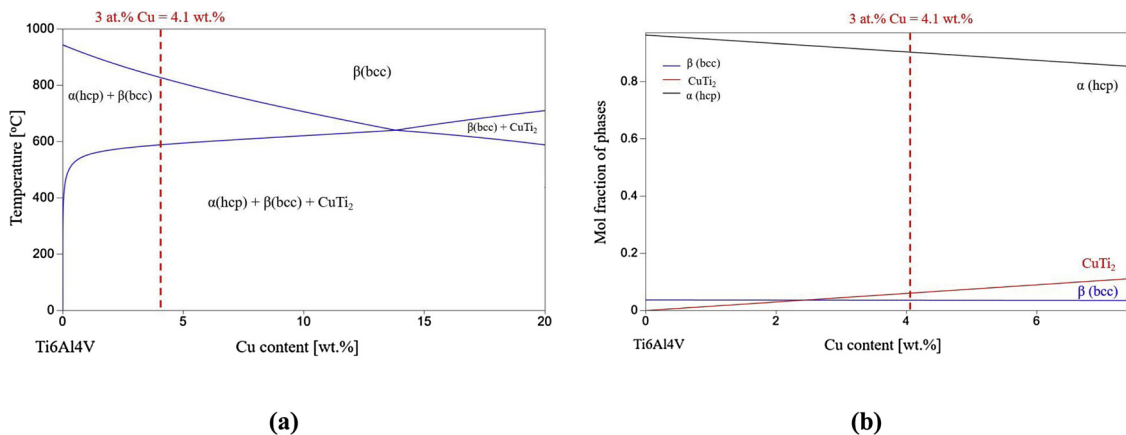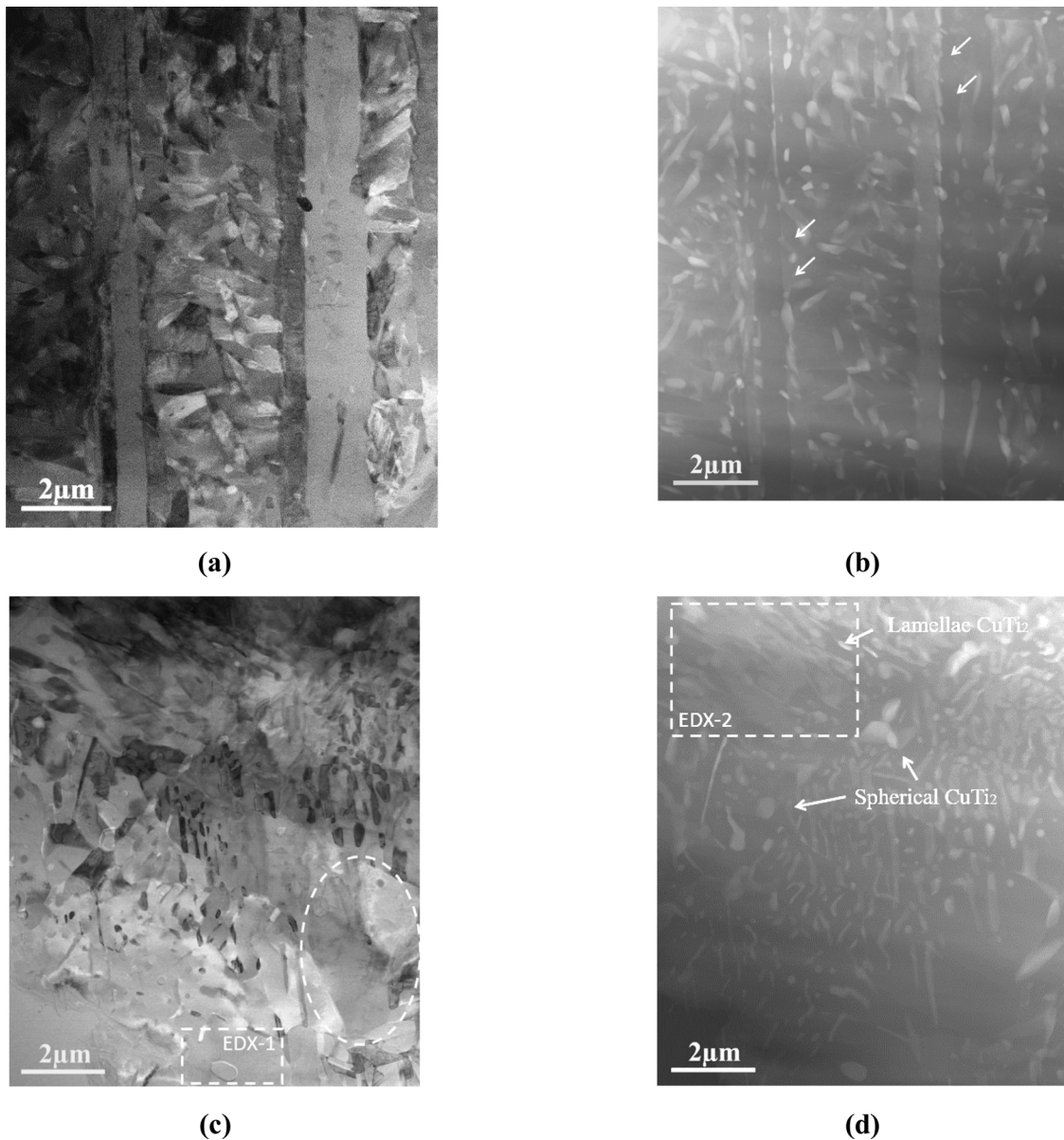

(a)   **(b)**

Fig. 6. (a) A section of (Ti–6 wt.% Al–4 wt.% V) + "x" wt.% Cu in a calculated Ti–Al–V–Cu quaternary phase diagram (b) and changes in mol fractions of constitute phases in equilibrium as a function of Cu content (wt.%) in studied compositions of Ti6Al4V-Cu at room temperature (25 °C).

(a)

(b)

(c)

(d)

Fig. 8. STEM – ADF and HADDF micrographs – of two different regions of L-PBF Ti6Al4V(ELI)-3 at.% Cu manufactured with a laser power of 170 W scanning speed of 0.7 m/s (a,b) region 1: low Cu areas (martensitic structure) and (c,d) region 2: high Cu areas.

dashed circle) [40]. Therefore, the high Cu content has a higher amount of CuTi$_2$ precipitates with spherical, as well as lamellae shape morphologies (dashed square, Fig. 8d).

Fig. 9a shows a high magnification micrograph of Fig. 8c (EDX-1, dashed-square). HR-STEM micrographs, together with their respective Fast Fourier Transformation (FFT), were used for the phase identification. Fig. 9 presents for each identified phase: (i) α/α´-phase (hcp-structure), (ii) β-phase (bcc-structure) and (iii) CuTi$_2$ intermetallic phase (tetragonal-structure). Observations suggested that CuTi$_2$ intermetallic precipitates have an incoherent interface with α/α´ and β phases, and a coherent interface between α/α´-β phases. The EDX mapping confirmed the presence of β-phase and CuTi$_2$ intermetallic phase due to the enrichment of V content, and Cu and Ti content, respectively (Fig. 9b). The EDX line profile along the particle confirmed the stoichiometry of CuTi$_2$ precipitates (Fig. 9c). Additionally, β-phase showed a percentage of around over 15 wt.% of V [41], but also the presence of 2.35 wt.% Cu.

Fig. 10 shows a higher magnification micrograph of Fig. 8d (EDX-2, dashed-square). This area showed different morphologies of CuTi$_2$

intermetallic phase, spherical and lamellae shapes. Spherical-shape particles were preferentially located at the interface between laths, while lamellae-shaped precipitates were preferentially located within the laths. On the other hand, the precipitation of β-phase nucleated between α' needles and was connected CuTi$_2$ intermetallic particles, probably due to copper as a β-phase stabilizer.

4. Discussion

4.1. Optimization of process parameters

4.1.1. Formation of single tracks

The shape of a single track is affected by the energy input and interaction time of the laser beam with the material. At excessive energy input due to high laser power or low scanning speed, single tracks became irregular, with a lot of attached satellite particles. In this case keyhole mode porosity was observed. At 170 W laser power and high scanning speeds, tracks became irregular, up to chains of beads (balling effect). Penetration depth into the substrate is highly important for
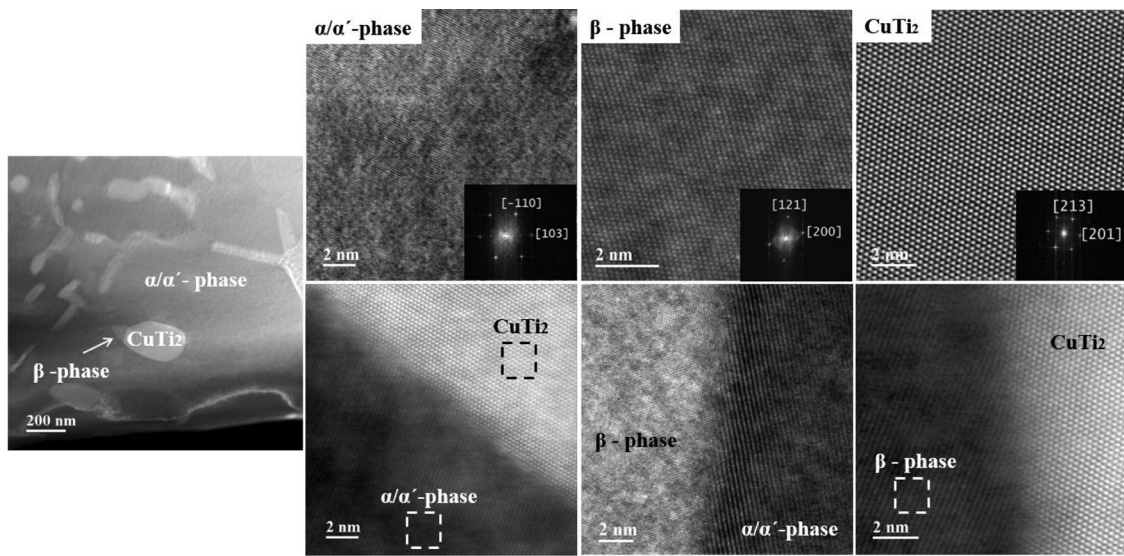
(a)
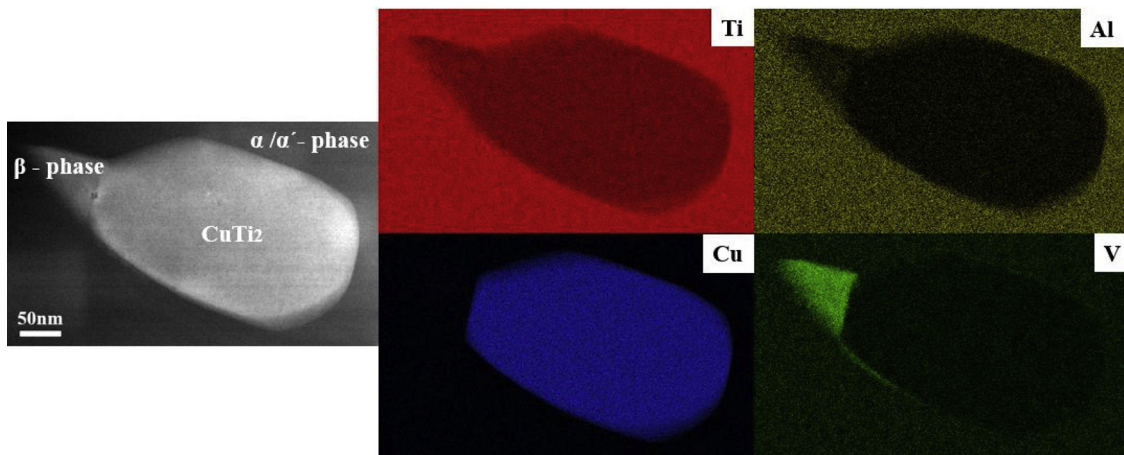
(b)
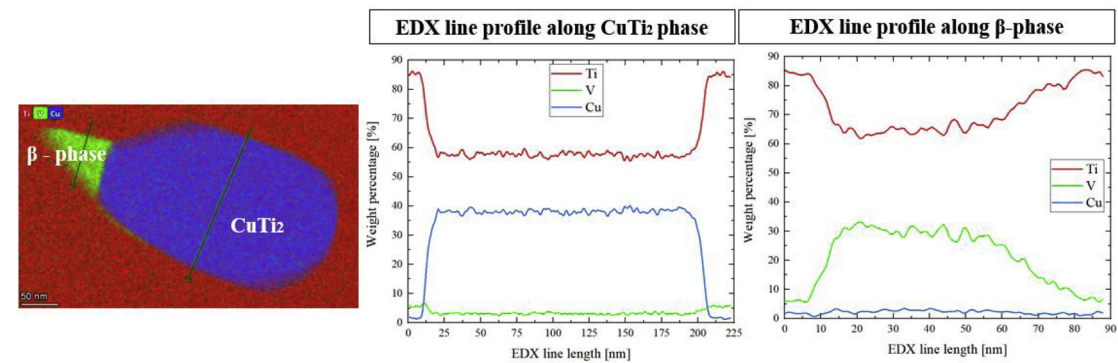
(c)

Fig. 9. (a) HR-STEM micrograph (area EDX-1, dashed-square at Fig. 8c) of α/α', β and $CuTi_2$ intermetallic phases with their respective FTT (insets), as well as the interface between α/α'- $CuTi_2$, α/α'- β, β - $CuTi_2$ phases suggesting their incoherency/coherency; (b) EDX mapping, showing the element distribution of Ti/Al/Cu/V ; (c) EDX line profiles along β-phase and $CuTi_2$ intermetallic phase.

reliable mechanical properties of fully dense L-PBF parts [42]. The regular shape of single tracks provides homogeneity of the layer which guarantees even deposition of powder layers, finally resulting in the production of dense parts with complex designs.

It must be noted that single tracks can be also continuous or discontinuous depending on the thickness of the powder layer. If the powder layer is too thick, the melting pool will not have contact with the substrate. It was previously reported that the optimal process parameters of single tracks Ti6Al4V(ELI) with a powder layer thickness of $15-45\,\mu m$ is a range of scanning speeds from 0.8 to 1.2 m / s and a
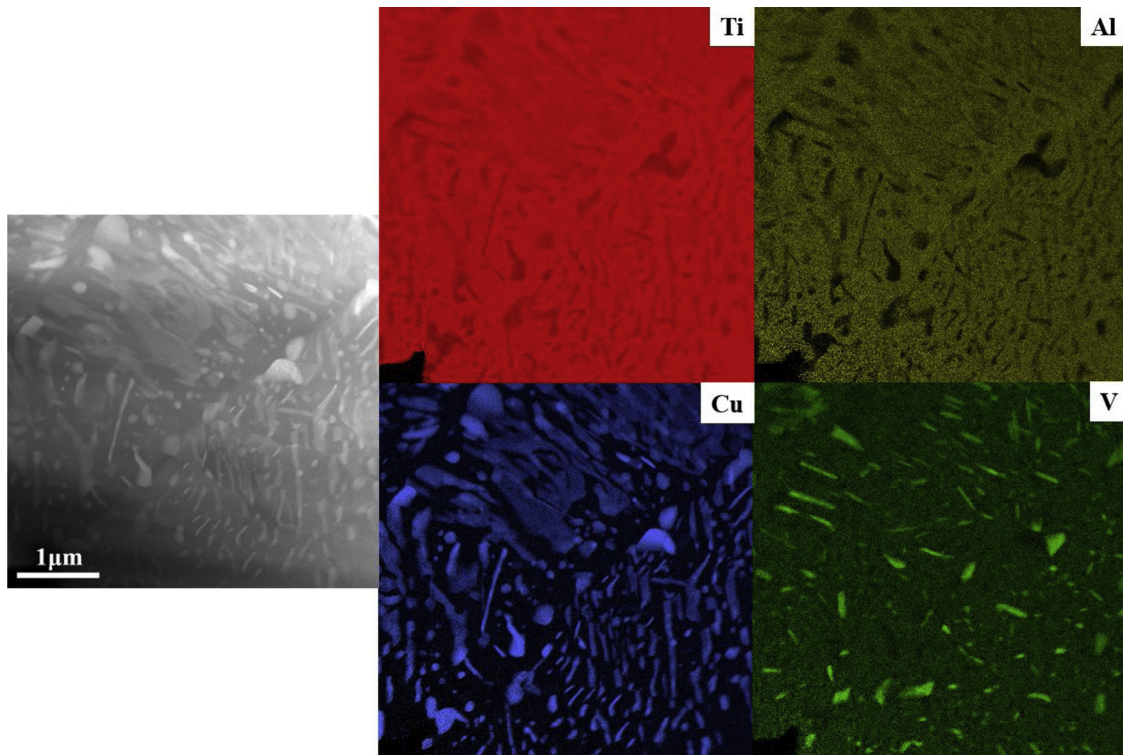
Fig. 10. EDX mapping (area EDX-2, dashed-square at Fig. 8d), showing the element distribution of Ti/Al/Cu/V, showing different morphologies of $CuTi_2$ intermetallic phase.

laser power of $150-170$ W [35]. In the present investigation, these findings were selected as a benchmark, but since Cu has lower absorption of laser radiation with 1075 nm wavelength, to melt a Ti6Al4V (ELI)- 3 at.% Cu mixture by laser with 170 W power, a lower scanning speed was chosen. It was necessary to ensure long enough interaction time between the laser beam and the powder/substrate material.

Similar to the finding for Ti6Al4V(ELI) [35], in the present investigation it was shown that stable single tracks were formed with scanning speeds below 1.4 m/s and laser power of 170 W, but also below scanning speeds of 1.6 m/s with laser power of 340 W. Humping and balling effects were found to start with higher laser scanning speeds, but at 340 W up to 2.8 m/s scanning speed, tracks were still continuous with $\sim 50\,\mu m$ penetration into the substrate. Observed irregularities and undercuts can provoke rough surfaces of single layers and finally, porosity in 3D parts. Experiments with single layers supported this assumption.

It must be noted that many satellites were observed near single tracks with both laser powers. The formation of satellites can be explained by the high thermal conductivity and lower melting point of Cu particles within the powder mixture. Due to high conductivity, heat from the track redistributed into the surrounding powder bed, and some particles partially melt and stick to the solidified track. Also, near 2000 °C the viscosity of molten pure Cu is half of that of Ti6Al4V [43,44], which means that the Ti6Al4V(ELI)-Cu powder mixture tends to generate more droplet spatters than Ti6Al4V(ELI) powder [45]. An influence of the process parameters on track geometry can be analyzed with respect of linear laser energy input P/V, where P is the laser power and V is the scanning speed. Figs. 11a and b show the relationship between the single track width and the laser penetration depth and the P/V ratio. It was observed that the single track width and penetration depth were quite similar for single tracks manufactured with the same linear laser energy input P/V, as was shown previously in [42]. The difference in penetration depth at higher linear energy input for different laser power can be explained considering the laser-matter interaction time (Fig. 11b). Fig. 11c illustrates the interaction time d/V,

where d is the laser spot diameter and V is the laser scanning speed for the investigated regimes. For longer interaction times, higher energy input caused higher maximum temperature, as well as lower viscosity of molten pool that provoked deep penetration up to the keyhole regime (Fig. 2a). For shorter interaction times, single tracks manufactured with a laser power of 340 W had a penetration depth deeper than 60 μm, but they were unstable, and their geometrical characteristics varied significantly (Fig. 11c). For situations with the same interaction time, single tracks appear more homogenous with a laser power of 340 W, but enriched copper areas were found near the edges of the tracks for both laser powers used (Fig. 12).

4.1.2. Formation of single layer

Surface roughness is an important factor influencing the quality of L-PBF parts because irregular surfaces can lead to a high deviation in the powder layer thickness. These variations can provoke lack-of-fusion porosity within the 3D part since the single layer melted previously is the substrate for the subsequent layer. The geometry of single tracks and denudation zones, together with hatch distance, makes the dependence of surface roughness on laser power and scanning speed quite complex (Fig. 3, Fig. 13). At the chosen hatch distance of 80 μm, single tracks overlap, and almost a half of the upper part of each single track was remelted during the manufacturing of a single layer with scanning speeds of 0.4–1.4 m/s and a laser power of 170 W. Therefore, the top surface of a single layer was very smooth at these process parameters (Fig. 13a). Apparently, higher copper concentration promoted lower viscosity and better wetting behavior of the molten pool.

A high laser energy input at 340 W laser power led to both a larger width of a single track and a wider denudation zone on the substrate. During the scanning of the first single track, the powder bed was regular and even, and when the laser beam was shifted by 80 μm, only the previously sintered single track and substrate (without or with a small amount of powder material due to denudation effect) melted (Fig. 13b, c) [42]. Since a solid surface has a lower laser absorbance than the powder material [46], a lower temperature was reached during this
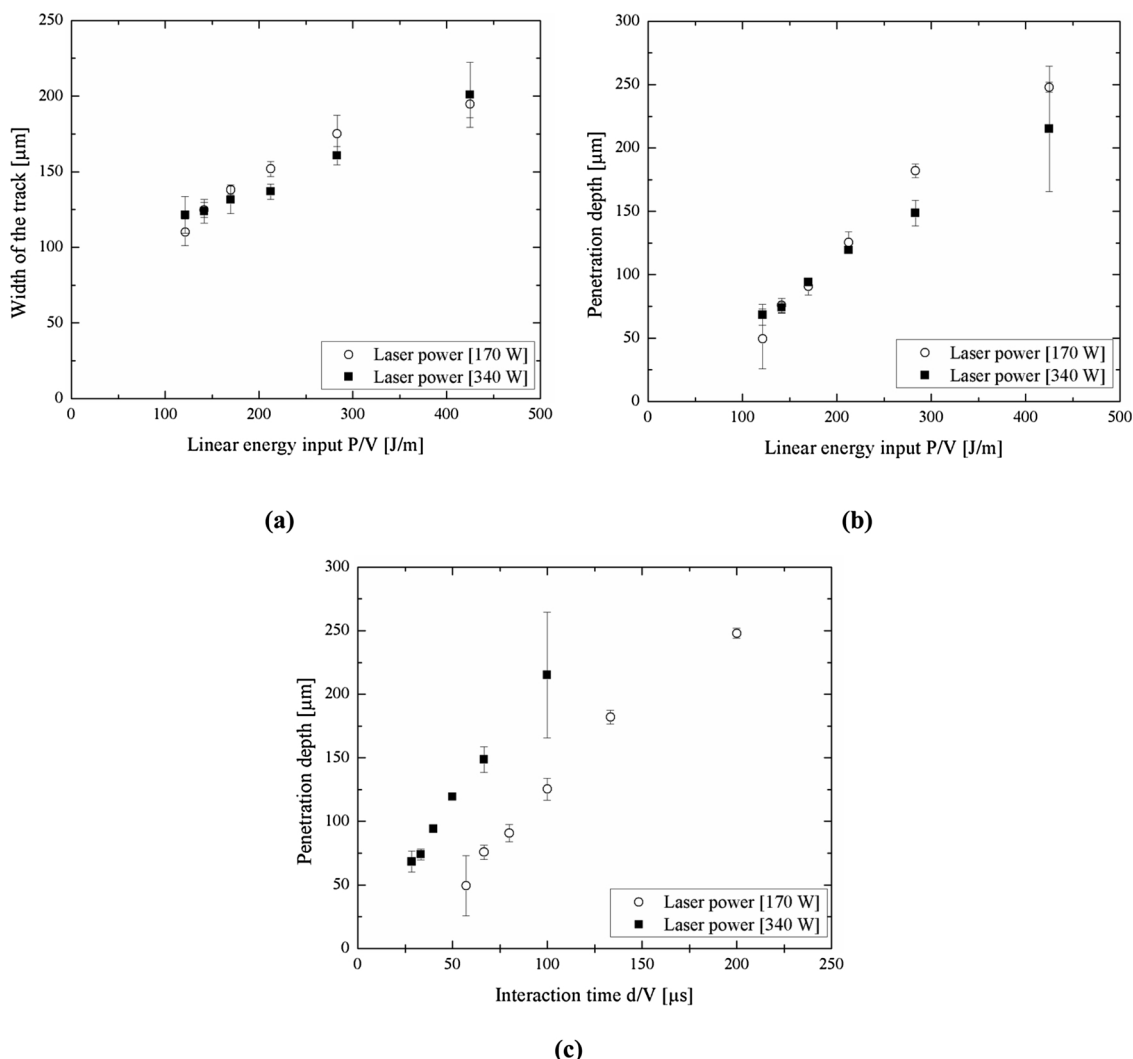
(a)

(b)

(c)

Fig. 11. Relationship between (a) width, (b) penetration depth of single tracks into the substrate *versus* linear energy input; (c) as well as penetration depth of single tracks *versus* interaction time.

process that, in turn, influenced the penetration depth and width of molten pool. It is also needed to keep in mind that the laser beam has already interacted not only with Ti6Al4V (substrate), but also with a new material Ti6Al4V-Cu (single track) with greater thermal conductivity and reflectivity; high concentration of Cu at the edges can increase reflection coefficient of laser radiation. The next scan again passes over a powder bed which is relatively regular, which in turn leads in the formation of a larger molten pool and larger denudation zone. This situation is repeated many times which results in a variation

of the penetration depth and track width during the manufacturing of a layer, Fig. 13b. Consecutive reduction of the powder consolidation zone and non-uniformity of tracks in single layer formation during PBF was shown for example, in [47–50] for L-PBF process and also for electron beam PBF [51]. Apparently, the combination of these specific process parameters led to such regular pattern, but this it was not optimal for the manufacturing of completely dense objects and was not subjected to thorough study.

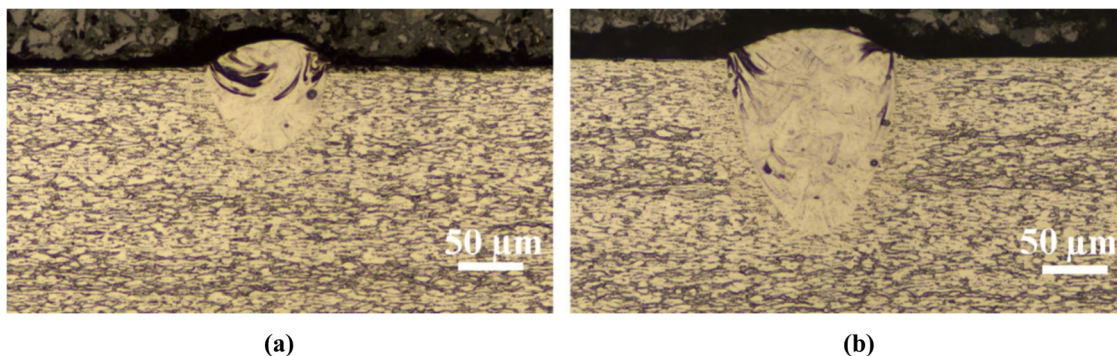With an increase in laser scanning speed at laser power of 340 W,

(a)

(b)

Fig. 12. Cross-sections of the single tracks with 1.2 m/s scanning speed with (a) 170 W and (b) 340 W laser power.
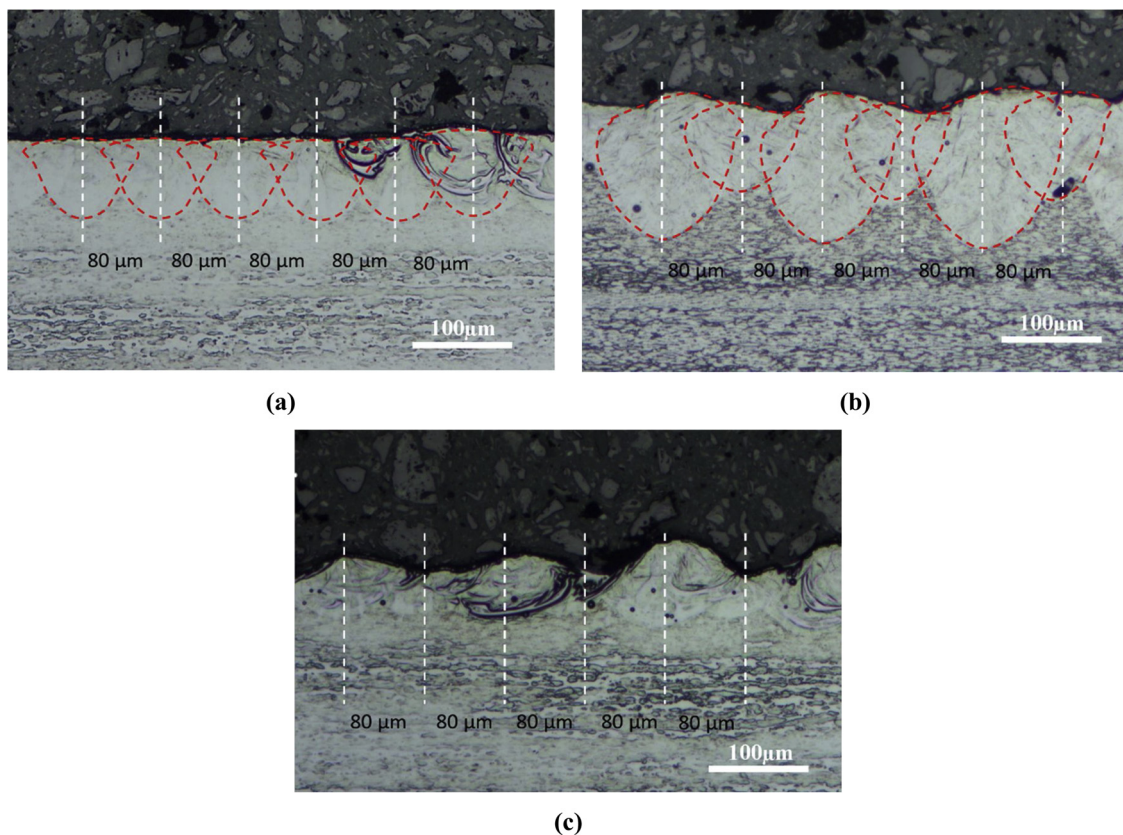
Fig. 13. Etched cross-sections of single layers manufactured with laser power and scanning speeds of (a) 170 W, 1.2 m/s, (b) 340 W, 1.6 m/s and, (c) 2.4 m/s.

humping effect also was observed. When humping with undercutting became very prominent, the surface of the melted layer was rough with high variations in Rz (Fig. 3, Fig. 13cc and). Lower scanning speeds showed smoother surfaces, due to the longer time for the melt pool existence and higher temperature, which promoted better wetting behavior. At higher laser power, the microstructure of single layers were more homogenous.

4.2. Evaluation of properties and microstructure of 3D cubes

Based on the experiments with single tracks and layers, a narrow range of scanning speeds was chosen for the manufacturing of 3D samples: $0.7 - 0.9$ m/s for 170 W and 1.0–1.2 m/s for 340 W. The selected process parameters allowed the manufacturing of 3D specimens with low porosity, which was confirmed by measurements using microCT and studies of cross sections by OM (Table 1, Fig. 4b).

The results of SEM EDX showed that full homogenization of the material was a challenge, but it was shown that this can be improved by an increase in laser power from 170 to 340 W. Experimental observations showed that an increased content of Cu in the solid solution decreased the highest concentration of Cu at fusion boundaries by a factor of two. These observations are in agreement with previously published results which showed that an increase in laser power can be used to increase the homogeneity of the L-PBF material [19,29,52].

STEM/EDX observations showed that the microstructure of L-PBF Ti6Al4V(ELI)-3 at.% Cu material corresponds well to XRD observations. The typical hexagonal α'-martensite phase was observed with needle like shape morphology. The observations confirmed the presence of β-phase mostly located between martensite laths, as well as the precipitation of $CuTi_2$ intermetallic phase. It is already known that XRD $< 110 >$ peak of cubic β titanium overlaps with $< 002 >$ peak of α/α'-phase, which makes it difficult to identify the cubic β-phase by XRD confidently. However, STEM and EDX allowed the confirmation of

those phases as well as the observation of their morphology, composition and location within the microstructure. Unfortunately, not many microstructural data has been reported on Ti6Al4V-Cu alloy, but microstructural features can be compared with the ones reported already reported for pure Ti-Cu alloy. Within literature, the presence of $CuTi_2$ intermetallic precipitates by conventional manufacturing methods (i.e. casting) by the addition of Cu between $1 - 10$ wt.% in pure Ti was reported in [8,16], but also for the Ti6Al4V alloy in [53,54]. According to the Ti-Cu binary equilibrium phase diagram, $CuTi_2$ intermetallic precipitates were found during conventional manufacturing due to the slow cooling rates; however, $CuTi_2$ precipitates were found to be unavoidable regardless the cooling rate applied [55]. The results in the present study showed that $CuTi_2$ precipitates were also achieved in Ti6Al4V-Cu alloy under the fast cooling rates of L-BPF manufacturing. Intermetallic precipitates may appear as the result of thermal cycling of the material during L-BPF manufacturing, where the material is subjected to multiple heating and cooling cycles as new layers are manufactured; on the other hand, due to the microsegregation and inhomogeneous microstructure within Ti6Al4V(ELI)-3 at.% Cu material, high Cu content regions could reach eutectoid composition presented in the quaternary equilibrium phase diagram. The eutectoid transformation in Ti-Cu binary system at 7.1 wt.% Cu was found to be independent from the cooling rates, and volume fractions of eutectoid structure and martensite depended on it [39]. At slow cooling rates, a defined lamellae structure, which is composed of lamellae of α and $CuTi_2$ lamellae, as well as α lamellae, was found. However, fast cooling rates, as well as the short time available for the formation of a defined lamellae structure during the diffusion process, led to the presence of a degenerate lamellar structure [39]. In the present study, the Ti6Al4V-Cu quaternary equilibrium phase diagram system showed a shift of the eutectoid point from 7.1 to ~ 14 wt.% Cu in comparison with Ti-Cu binary system. Regions with lamellar $CuTi_2$ intermetallic phase can be observed in the material (Fig. 10). However, it is hard to predict if

eutectoid reaction can take place with the faster L-PBF cooling rates but also with Ti6Al4V(ELI) alloy. A recent study on pure Ti-8.5 wt.% Cu by L-PBF achieved a fully equiaxed ultrafine-eutectoid microstructure [56]. It is already known that the intrinsic high cooling rates and high thermal gradients of the L-PBF often leads to a very fine microstructure composed by columnar grains. However, authors reported that the thermal history of Ti-Cu L-BPF accumulated heat during the deposition of the successive layers reducing the cooling rate and $\beta \rightarrow \alpha + CuTi_2$ was completed before the martensite transformation was reached. Also, authors demonstrated the high constitutional supercooling capacity of Ti-Cu alloys can override the negative effect of high thermal gradients during the manufacturing [56]. Due to that, fully equiaxed microstructure was obtained. In the present study, *in-situ* alloying of Ti6Al4V (ELI)-3 at.% Cu led to a columnar prior β-grain microstructure, were martensite was obtained after the L-PBF process. Compared to [56], the presence of Al and V alloying elements in Ti6Al4V alloy as well as the use of different process parameters influenced the final microstructure. Even so, the nucleation of β- and $CuTi_2$ phases within the microstructure were found. They were observed to be connected to each other, probably due to the diffusion process of Cu atoms between β and $CuTi_2$ phases, as Cu is a β-stabilizer. However, further research needs to be performed to confirm the nucleation mechanism of β and $CuTi_2$ phases in Ti6Al4V-Cu alloys.

Vickers hardness of Ti6Al4V(ELI)-3 at.% Cu samples produced with laser powers of 170 W and 340 W and after stress-relieving heat treatment were similar ($HV_{0.2}$ 459 $\pm$ 7 and 460 $\pm$ 11 correspondingly), and higher than stress-relieved LPBF Ti6Al4V(ELI) samples ($HV_{0.2}$ 374 $\pm$ 17) found in previous work [57]. The increase in hardness of Ti6Al4V(ELI)-3 at.% Cu in comparison with pure Ti6Al4V(ELI) was likely caused by very fine martensite phase and $CuTi_2$ intermetallic phase formation. Other studies regarding mechanical properties of Ti6Al4V-Cu alloys manufactured by casting also reported the increase in hardness with the addition of Cu content, from $HV_{0.1}$ 358 to $HV_{0.1}$ 506, by increasing Cu content from 1 to 10 wt.% Cu. However, a significant reduction of tensile strength from 1016 to 387 MPa was observed [58], suggesting that in order to obtain good mechanical properties, only small amounts of Cu ($1-4$ wt.%) should be used.

5. Conclusions

This article presents the feasibility of *in-situ* alloying Ti6Al4V(ELI)-3 at.% Cu material by L-PBF for biomedical applications. A hierarchical approach to develop optimal process parameters was performed by the analysis of single tracks, single layers and 3D samples. To summarize:

1 Optimal process parameters for the 3D *in-situ* alloyed Ti6Al4V(ELI)-3 at.% Cu samples were found to be with laser powers of 170 W and 340 W and scanning speeds of $0.7-0.9$ m/s and 1.0–1.2 m/s, respectively. A verification of low porosity and homogeneity was performed. Densities of 99.98 % and higher than 99.99 % were correspondingly confirmed by microCT scans.

2 *In-situ* L-PBF alloying was challenging and a homogeneous distribution of Cu within the alloy was not achieved. An increase in laser power from 170 to 340 W, resulted in some homogenization effect, but at the same time, an increase in Cu content in the solid solution and almost half of the highest concentration of Cu at fusion boundaries were observed in materials manufactured with a laser power of 340 W.

3 Microstructural analyses showed that the Ti6Al4V(ELI)-3 at.% Cu was composed of three phases: α' and β phases, as well as $CuTi_2$ intermetallic precipitates. STEM observations showed two main regions within the material, with low and high Cu contents. The first region was dominant, corresponding to a martensitic structure, where β-phase and $CuTi_2$ spherical-like shape morphologies were found to be preferentially located between α' needles. The second region was coarser, where round α grains were found. This second region showed larger areas with different morphologies (spherical and lamellae shapes) of $CuTi_2$ intermetallic phase. Spherical-shape particles were preferentially located at the interface between laths, while lamellae-shaped precipitates were preferentially located within the laths. On the other hand, the precipitation of β-phase nucleated between α' needles and was connected $CuTi_2$ intermetallic particles, probably due to copper as a β-phase stabilizer.

4 The fine microstructure with the $CuTi_2$ intermetallic phase precipitates resulted in an increase in hardness of the *in-situ* L-PBF Ti6Al4V(ELI)-3 at.% Cu to ($HV_{0.2}$ 459 $\pm$ 7 and 460 $\pm$ 11 with laser powers of 170 W and 340 W, correspondingly), which was higher than the microhardness of stress-relieved Ti6Al4V(ELI) samples ($HV_{0.2}$ 374 $\pm$ 17) reported in previous work.

5 It was demonstrated that in-situ L-PBF alloying can be a promising method for obtaining new materials with additional useful properties.

6 Future extensions of the work should be conducted on mechanical and biological properties to ensure mechanical property requirements, as well as good cellular response and antibacterial effect of *in-situ* alloyed Ti6AL4V(ELI)-3 at.% Cu for biomedical application.

7 A comparative study of the antibacterial effectiveness of pre-alloyed and *in-situ* alloyed titanium-copper L-PBF material and appropriate heat treatment have to be done.

CRediT authorship contribution statement

A.M. Vilardell: Investigation, Data curation, Writing - original draft, Writing - review & editing, Visualization, Project administration, Funding acquisition. **I. Yadroitsev:** Conceptualization, Methodology, Investigation, Validation, Resources, Writing - original draft, Writing - review & editing, Supervision, Project administration, Funding acquisition. **I. Yadroitsava:** Conceptualization, Methodology, Investigation, Formal analysis, Validation, Writing - original draft, Writing - review & editing, Supervision, Project administration, Funding acquisition. **M. Albu:** Investigation, Resources, Writing - original draft. **N. Takata:** Investigation, Resources, Writing - review & editing. **M. Kobashi:** Resources. **P. Krakhmalev:** Conceptualization, Investigation, Resources, Writing - review & editing, Supervision, Funding acquisition. **D. Kouprianoff:** Investigation, Validation. **G. Kothleitner:** Resources. **A. du Plessis:** Validation, Investigation, Writing - original draft, Writing - review & editing, Supervision.

Declaration of Competing Interest

One of the authors of this article is part of the editorial board of the journal. To avoid potential conflicts of interest, the responsibility for the editorial and peer-review process of this article lies with the other editors of the journal. Furthermore, the authors of this article were removed from the peer review process and have no access to confidential information related to the editorial process of this article.

Acknowledgements

References

[1] G.F.M. Gad, A.A.A. Azis, R. AlyIbrahem, In-vitro adhesion of Staphylococcus spp. to certain orthopedic biomaterials and expression of adhesion genes, J. Appl. Pharm. Sci. 06 (2012) 145–149, https://doi.org/10.7324/JAPS.2012.2634.

[2] S. Guo, Y. Lu, S. Wu, L. Liu, M. He, C. Zhao, Y. Gan, J. Lin, J. Luo, X. Xu, J. Lin, Preliminary study on the corrosion resistance, antibacterial activity and cytotoxicity of selective-laser-melted Ti6Al4V- x Cu alloys, Mate. Sci. Eng. C 72 (2017) 631–640, https://doi.org/10.1016/j.msec.2016.11.126.

[3] D. Tigani, D. Dallari, C. Coppola, R. Ben Ayad, G. Sabbioni, M. Fosco, Total knee arthroplasty for post-traumatic proximal tibial bone defect: three cases report, Open Orthop. J. 5 (2011) 143–150, https://doi.org/10.2174/1874325001105010143.

[4] Y. Zheng, X. Xu, Z. Xu, J. Wang, H. Cai, Metallic Biomaterials: New Directions and Technologies, Wiley-VCH Verlag GmbH & Co. KGaA, Weinheim, Germany, 2017, https://doi.org/10.1002/9783527342440.

[5] J. Liu, F. Li, C. Liu, H. Wang, B. Ren, K. Yang, E. Zhang, Effect of Cu content on the antibacterial activity of titanium–copper sintered alloys, Mater. Sci. Eng. C 35 (2014) 392–400, https://doi.org/10.1016/j.msec.2013.11.028.

[6] E. Zhang, F. Li, H. Wang, J. Liu, C. Wang, M. Li, K. Yang, A new antibacterial titanium–copper sintered alloy: preparation and antibacterial property, Mater. Sci. Eng. C 33 (2013) 4280–4287, https://doi.org/10.1016/j.msec.2013.06.016.

[7] Z. Ma, M. Yao, R. Liu, K. Yang, L. Ren, Y. Zhang, Z. Liao, W. Liu, M. Qi, Study on antibacterial activity and cytocompatibility of Ti–6Al–4V–5Cu alloy, Mater. Technol. 30 (2015) B80–B85, https://doi.org/10.1179/1753555714Y. 0000000237.

[8] R. Liu, K. Memarzadeh, B. Chang, Y. Zhang, Z. Ma, R.P. Allaker, L. Ren, K. Yang, Antibacterial effect of copper-bearing titanium alloy (Ti-Cu) against Streptococcus mutans and Porphyromonas gingivalis, Sci Rep. 6 (2016) 29985, https://doi.org/10.1038/srep29985.

[9] M. Li, L. Nan, D. Xu, G. Ren, K. Yang, Antibacterial performance of a Cu-bearing stainless steel against microorganisms in tap water, J. Mater. Sci. Technol. 31 (2015) 243–251, https://doi.org/10.1016/j.jmst.2014.11.016.

[10] X. Jin, L. Gao, E. Liu, F. Yu, X. Shu, H. Wang, Microstructure, corrosion and tribological and antibacterial properties of Ti–Cu coated stainless steel, J. Mech. Behav. Biomed. Mater. 50 (2015) 23–32, https://doi.org/10.1016/j.jmbbm.2015. 06.004.

[11] Q. Wang, L. Ren, X. Li, S. Zhang, T.B. Sercombe, K. Yang, Antimicrobial Cu-bearing stainless steel scaffolds, Mater. Sci. Eng. C 68 (2016) 519–522, https://doi.org/10. 1016/j.msec.2016.06.038.

[12] D. Sun, D. Xu, C. Yang, M.B. Shahzad, Z. Sun, J. Xia, J. Zhao, T. Gu, K. Yang, G. Wang, An investigation of the antibacterial ability and cytotoxicity of a novel cu-bearing 317L stainless steel, Sci Rep. 6 (2016) 29244, https://doi.org/10.1038/ srep29244.

[13] Y.-H. Song, M.-K. Kim, E.-J. Park, H.-J. Song, K.J. Anusavice, Y.-J. Park, Cytotoxicity of alloying elements and experimental titanium alloys by WST-1 and agar overlay tests, Dent. Mater. 30 (2014) 977–983, https://doi.org/10.1016/j. dental.2014.05.012.

[14] X. Wang, H. Dong, J. Liu, G. Qin, D. Chen, E. Zhang, In vivo antibacterial property of Ti-Cu sintered alloy implant, Mater. Sci. Eng C 100 (2019) 38–47, https://doi. org/10.1016/j.msec.2019.02.084.

[15] L. Fowler, O. Janson, H. Engqvist, S. Norgren, C. Öhman-Mägi, Antibacterial investigation of titanium-copper alloys using luminescent Staphylococcus epidermidis in a direct contact test, Mater. Sci. Eng.: C 97 (2019) 707–714, https://doi.org/10. 1016/j.msec.2018.12.050.

[16] Y. Alshammari, F. Yang, L. Bolzoni, Low-cost powder metallurgy Ti-Cu alloys as a potential antibacterial material, J. Mech. Behav. Biomed. Mater. 95 (2019) 232–239, https://doi.org/10.1016/j.jmbbm.2019.04.004.

[17] X. Xu, Y. Lu, S. Li, S. Guo, M. He, K. Luo, J. Lin, Copper-modified Ti6Al4V alloy fabricated by selective laser melting with pro-angiogenic and anti-inflammatory properties for potential guided bone regeneration applications, Mate. Sci. Eng C 90 (2018) 198–210, https://doi.org/10.1016/j.msec.2018.04.046.

[18] D. Campoccia, L. Montanaro, C.R. Arciola, The significance of infection related to orthopedic devices and issues of antibiotic resistance, Biomaterials 27 (2006) 2331–2339, https://doi.org/10.1016/j.biomaterials.2005.11.044.

[19] P. Krakhmalev, I. Yadroitsev, I. Yadroitsava, O. de Smidt, Functionalization of biomedical Ti6Al4V via in situ alloying by Cu during laser powder bed fusion manufacturing, Materials 10 (2017) 1154, https://doi.org/10.3390/ma10101154.

[20] I. Yadroitsava, A. du Plessis, I. Yadroitsev, Bone regeneration on implants of titanium alloys produced by laser powder bed fusion: a review, Titanium for Consumer Applications, Elsevier, 2019, pp. 197–233, https://doi.org/10.1016/B978-0-12-815820-3.00016-2.

[21] A. du Plessis, I. Yadroitsev, I. Yadroitsava, S.G. Le Roux, X-ray microcomputed tomography in additive manufacturing: a review of the current technology and applications, 3D Printing Addit. Manuf. 5 (2018) 227–247, https://doi.org/10. 1089/3dp.2018.0060.

[22] T. DebRoy, H.L. Wei, J.S. Zuback, T. Mukherjee, J.W. Elmer, J.O. Milewski, A.M. Beese, A. Wilson-Heid, A. De, W. Zhang, Additive manufacturing of metallic components – process, structure and properties, Prog. Mater. Sci. 92 (2018) 112–224, https://doi.org/10.1016/j.pmatsci.2017.10.001.

[23] I. Yadroitsev, P. Krakhmalev, I. Yadroitsava, Hierarchical design principles of selective laser melting for high quality metallic objects, Addit. Manuf. 7 (2015) 45–56, https://doi.org/10.1016/j.addma.2014.12.007.

[24] S. Dadbakhsh, L. Hao, In situ formation of particle reinforced Al matrix composite by selective laser melting of Al/Fe2O3 powder mixture, Adv. Eng. Mater. 14 (2012) 45–48, https://doi.org/10.1002/adem.201100151.

[25] S. Dadbakhsh, R. Mertens, K. Vanmeensel, J. Vleugels, J.V. Humbeeck, J.-P. Kruth, In situ alloying and reinforcing of Al6061 during selective laser melting, Procedia CIRP 74 (2018) 39–43, https://doi.org/10.1016/j.procir.2018.08.009.

[26] M.L. Montero-Sistiaga, R. Mertens, B. Vrancken, X. Wang, B. Van Hooreweder, J.-P. Kruth, J. Van Humbeeck, Changing the alloy composition of Al7075 for better processability by selective laser melting, J. Mater. Process. Technol. 238 (2016) 437–445, https://doi.org/10.1016/j.jmatprotec.2016.08.003.

[27] M. Simonelli, N.T. Aboulkhair, P. Cohen, J.W. Murray, A.T. Clare, C. Tuck, R.J.M. Hague, A comparison of Ti-6Al-4V in-situ alloying in selective laser melting using simply-mixed and satellited powder blend feedstocks, Mater. Charact. 143 (2018) 118–126, https://doi.org/10.1016/j.matchar.2018.05.039.

[28] P. Krakhmalev, I. Yadroitsev, I. Baker, I. Yadroitsava, Manufacturing of intermetallic Mn-46%Al by laser powder bed fusion, Procedia CIRP 74 (2018) 64–67, https://doi.org/10.1016/j.procir.2018.08.031.

[29] P. Krakhmalev, I. Yadroitsev, Microstructure and properties of intermetallic composite coatings fabricated by selective laser melting of Ti–SiC powder mixtures, Intermetallics 46 (2014) 147–155, https://doi.org/10.1016/j.intermet.2013.11. 012.

[30] A. du Plessis, P. Sperling, A. Beerlink, L. Tshabalala, S. Hoosain, N. Mathe, S.G. le Roux, Standard method for microCT-based additive manufacturing quality control 1: porosity analysis, MethodsX 5 (2018) 1102–1110, https://doi.org/10.1016/j. mex.2018.09.005.

[31] P. Schlossmacher, D.O. Klenov, B. Freitag, H.S. von Harrach, Enhanced detection sensitivity with a new windowless XEDS system for AEM based on silicon drift detector technology, Microsc. Today 18 (2010) 14–20.

[32] J.I. Goldstein, D.B. Williams, G. Cliff, Quantification of energy dispersive spectra, in: D.C. Joy, A.D. Romig, J.L. Goldstein (Eds.), Principles of Analytical Electron Microscopy, Plenum Press, New York, 1986, pp. 155–217.

[33] Y.A. Chang, S. Chen, F. Zhang, X. Yan, F. Xie, R. Schmid-Fetzer, W.A. Oates, Phase diagram calculation: past, present and future, Prog. Mater. Sci. 49 (2004) 313–345, https://doi.org/10.1016/S0079-6425(03)00025-2.

[34] CompuTherm LLC, CompuTherm Database User'S Guide, (2016), pp. 1–11 http:// www.computherm.com/download/Database2016_Manual.pdf.

[35] I. Yadroitsava, J. Els, G. Booysen, I. Yadroitsev, Peculiarities of single track formation from Ti6Al4V alloy at different laser power densities by selective laser melting, SAJIE 26-3 (2015), https://doi.org/10.7166/26-3-1185.

[36] P. Krakhmalev, G. Fredriksson, I. Yadroitsava, N. Kazantseva, A. du Plessis, I. Yadroitsev, Deformation behavior and microstructure of Ti6Al4V manufactured by SLM, Phys. Procedia 83 (2016) 778–788, https://doi.org/10.1016/j.phpro.2016. 08.080.

[37] I. Yadroitsev, P. Krakhmalev, I. Yadroitsava, A. Du Plessis, Qualification of Ti6Al4V ELI alloy produced by laser powder bed fusion for biomedical applications, JOM 70 (2018) 372–377, https://doi.org/10.1007/s11837-017-2655-5.

[38] M.H. Mueller, H.W. Knott, The crystal structures of Ti2Cu, Ti2Ni, Ti4Cu20, Trans. Metall. Soc. AIME 227 (1963) 674–678.

[39] S.A. Souza, C.R.M. Afonso, P.L. Ferrandini, A.A. Coelho, R. Caram, Effect of cooling rate on Ti–Cu eutectoid alloy microstructure, Mater. Sci. Eng. C 29 (2009) 1023–1028, https://doi.org/10.1016/j.msec.2008.09.007.

[40] M.-W. Wu, P.-H. Lai, The positive effect of hot isostatic pressing on improving the anisotropies of bending and impact properties in selective laser melted Ti-6Al-4V alloy, Mater. Sci. Eng. A 658 (2016) 429–438, https://doi.org/10.1016/j.msea. 2016.02.023.

[41] Ti-6Al-4V, in: Rodney Boyer, Gerhard Welsch, E.W. Collings (Eds.), Materials Properties Handbook: Titanium Alloys, 2020, p. 490 ISBN-10: 0-87180-481-1.

[42] I. Yadroitsev, Selective Laser Melting: Direct Manufacturing of 3D-Objects by Selective Laser Melting of Metal Powders, Lambert Acad. Publ, Saarbrücken, 2009.

[43] P.-F. Paradis, T. Ishikawa, S. Yoda, Non-contact measurements of surface tension and viscosity of niobium, zirconium, and titanium using an electrostatic levitation furnace, Int. J. Thermophys. 23 (2002) 825–842, https://doi.org/10.1023/ A:1015459222027.

[44] M.J. Assael, A.E. Kalyva, K.D. Antoniadis, R. Michael Banish, I. Egry, J. Wu, E. Kaschnitz, W.A. Wakeham, Reference data for the density and viscosity of liquid copper and liquid Tin, J. Phys. Chem. Ref. Data 39 (2010) 033105, https://doi.org/ 10.1063/1.3467496.

[45] C.L.A. Leung, S. Marussi, M. Towrie, J. del Val Garcia, R.C. Atwood, A.J. Bodey, J.R. Jones, P.J. Withers, P.D. Lee, Laser-matter interactions in additive manufacturing of stainless steel SS316L and 13-93 bioactive glass revealed by in situ X-ray imaging, Addit. Manuf. 24 (2018) 647–657, https://doi.org/10.1016/j.addma. 2018.08.025.

[46] Y. Yang, D. Gu, D. Dai, C. Ma, Laser energy absorption behavior of powder particles using ray tracing method during selective laser melting additive manufacturing of aluminum alloy, Mater. Des. 143 (2018) 12–19, https://doi.org/10.1016/j.matdes. 2018.01.043.

[47] I. Yadroitsev, I. Smurov, Surface morphology in selective laser melting of metal powders, Phys. Procedia 12 (2011) 264–270, https://doi.org/10.1016/j.phpro. 2011.03.034.

[48] A. Liebisch, M. Merkel, On the numerical simulation of the thermal behavior during the selective laser melting process, Materialwiss. Werkst. 47 (2016) 521–529, https://doi.org/10.1002/mawe.201600528.

[49] Y.-L. Guo, L.-N. Jia, B. Kong, Y.-L. Huang, H. Zhang, Energy density dependence of bonding characteristics of selective laser-melted Nb–Si-based alloy on titanium substrate, Acta. Metall. Sin. (Engl. Lett.) 31 (2018) 477–486, https://doi.org/10.1007/s40195-017-0670-8.

[50] Y. Guo, L. Jia, B. Kong, N. Wang, H. Zhang, Single track and single layer formation in selective laser melting of niobium solid solution alloy, Chin. J. Aeronaut. 31 (2018) 860–866, https://doi.org/10.1016/j.cja.2017.08.019.

[51] P. Karimi, E. Sadeghi, P. Åkerfeldt, J. Ålgårdh, J. Andersson, Influence of successive thermal cycling on microstructure evolution of EBM-manufactured alloy 718 in track-by-track and layer-by-layer design, Mater. Des. 160 (2018) 427–441, https://doi.org/10.1016/j.matdes.2018.09.038.

[52] I. Yadroitsev, P. Krakhmalev, I. Yadroitsava, Titanium alloys manufactured by in situ alloying during laser powder bed fusion, JOM 69 (2017) 2725–2730, https://doi.org/10.1007/s11837-017-2600-7.

[53] L. Ren, Z. Ma, M. Li, Y. Zhang, W. Liu, Z. Liao, K. Yang, Antibacterial properties of Ti–6Al–4V–xCu alloys, J. Mater. Sci. Technol. 30 (2014) 699–705, https://doi.org/10.1016/j.jmst.2013.12.014.

[54] C. Peng, Y. Liu, H. Liu, S. Zhang, C. Bai, Y. Wan, L. Ren, K. Yang, Optimization of annealing treatment and comprehensive properties of Cu-containing Ti6Al4V-xCu alloys, J. Mater. Sci. Technol. 35 (2019) 2121–2131, https://doi.org/10.1016/j.jmst.2019.05.020.

[55] F.F. Cardoso, A. Cremasco, R.J. Contieri, E.S.N. Lopes, C.R.M. Afonso, R. Caram, Hexagonal martensite decomposition and phase precipitation in Ti–Cu alloys, Mater. Des. 32 (2011) 4608–4613, https://doi.org/10.1016/j.matdes.2011.03.040.

[56] D. Zhang, D. Qiu, M.A. Gibson, Y. Zheng, H.L. Fraser, D.H. StJohn, M.A. Easton, Additive manufacturing of ultrafine-grained high-strength titanium alloys, Nature 576 (2019) 91–95, https://doi.org/10.1038/s41586-019-1783-1.

[57] M.G. Moletsane, P. Krakhmalev, N. Kazantseva, A. du Plessis, I. Yadroitsava, I. Yadroitsev, Tensile properties and microstructure of direct metal laser-sintered Ti6Al4V (ELI) alloy, S. Afr. J. Ind. Eng. 27 (2016), https://doi.org/10.7166/27-3-1667.

[58] T. Aoki, I.C.I. Okafor, I. Watanabe, M. Hattori, Y. Oda, T. Okabe, Mechanical properties of cast Ti-6Al-4V-XCu alloys, J. Oral Rehabil. 31 (2004) 1109–1114, https://doi.org/10.1111/j.1365-2842.2004.01347.x.